Lowest accreting protoplanetary discs as diagnostic of disc dispersal

Barbara Ercolano,[1,2]* Giovanni Picogna[1] and Kristina Monsch[3]

[1] *University Observatory, Faculty of Physics, Ludwig-Maximilians-Universität München, Scheinerstr. 1, 81679 Munich, Germany*

[2] *Exzellenzcluster 'Origins', Boltzmannstr. 2, 85748 Garching, Germany*

[3] *Harvard-Smithsonian Center for Astrophysics, 60 Garden Street, Cambridge MA 02138, USA*

ABSTRACT

The lowest accreting .....

Key words: keyword1 – keyword2 – keyword3

1 INTRODUCTION

Circumstellar disks are studied since more than 40 years, though the mechanism responsible for their evolution and final dispersal remains elusive (see for recent reviews Pascucci et al. 2022; Lesur et al. 2022). It has been determined observationally that the disc fraction of accreting pre-main-sequence stars decreases with the age of the population (see e.g. Mamajek 2009), while having ∼ 10% of non-accreting star bearing discs (Skrutskie et al. 1990).

The transition between accreting and non-accreting stars plays an important role in determining the final architecture of the forming planetary systems, as the speed of this process can cut out the supply for forming giant planets and halt their migration (see e.g. Monsch et al. 2019).

Thanathibodee et al. (2022) recently looked for an accretion signatures in disc-bearing stars previously thought to be non-accretors, using the He I λ10830Å line. This high excitation line allowed them to probe material in the innermost regions of protostellar discs, possibly detecting accretion streamers. They found that a large fraction of this sample (at least $20 - 30\%$) indeed shows signs of accretion via strong red-shifted absorption consistent with free-fall velocities, preferentially at young ages and almost independently of the stellar mass. The accretion rates were then determined independently by fitting the H-α profiles, of a sub-sample of these stars, using magnetospheric accretion models (Thanathibodee et al. 2023). Interestingly, although the statistics was very low (24 sources), the authors derived a minimum accretion rate of the order of 10^{-10} M$_\odot$ yr^{-1}, even though their method was able to detect rates 5 to 10 times lower, hinting some physical rather than selection limit. They further suggested that, since this rate is similar to the mass-loss rate provided by classical models of EUV photoevaporation (see e.g. Alexander & Armitage 2007), this mechanism of disc dispersal is a viable candidate to explain the transition between an accreting and non-accreting disc.

In this paper we test this hypothesis by producing synthetic populations of viscously evolving discs dispersed by photoevaporation, testing the different scenarios of EUV- and X-ray photoevaporation.

In Section 2 we describe the method adopted, and in Section 3 we present the result and draw the conclusions in Section 4.

2 METHODS

We use the one-dimensional viscous evolution code SPOCK (Ercolano & Rosotti 2015) which evolves the gas following

$$\frac{\partial \Sigma}{\partial t} = \frac{1}{R}\frac{\partial}{\partial R}\left[3R^{1/2}\frac{\partial}{\partial R}(\nu\Sigma R^{1/2})\right] - \dot{\Sigma}_w(R,t)\,, \qquad (1)$$

where the first term on the right hand side describes the viscous disc evolution (Lynden-Bell & Pringle 1974), and the second one is a sink term modelling the mass-loss due to internal disc photoevaporation.

We consider either an EUV or X-ray mass-loss rate internal photoevaporation profiles as they are well-studied in literature, and simple 1D presciptions of the disc mass-loss rates are provided.

2.1 X-ray photoevaporation

The XEUV surface mass-loss rate is given following Picogna et al. (2019)

$$
\begin{aligned}
\dot{\Sigma}_{\mathrm{XEUV}}(R) \quad &= \ln(10)\Bigg(\frac{6\,a\,\ln(R)^5}{R\ln(10)^6} + \frac{5\,b\,\ln(R)^4}{R\ln(10)^5} + \frac{4\,c\,\ln(R)^3}{R\ln(10)^4} + \quad (2)\\
&\quad \frac{3\,d\,\ln(R)^2}{R\ln(10)^3} + \frac{2\,e\,\ln(R)}{R\ln(10)^2} + \\
&\quad \frac{f}{R\ln(10)}\Bigg)\frac{\dot{M}_{\mathrm{XEUV}}(R)}{2\pi R}\,,
\end{aligned}
$$

where

$$\frac{\dot{M}_{\mathrm{XEUV}}(R)}{\dot{M}_{\mathrm{XEUV}}(M_\star, L_{X,\mathrm{soft}})} = 10^{a\log R^6 + b\log R^5 + c\log R^4 + d\log R^3 + e\log R^2 + f\log R + g} \qquad (3)$$

and the parameters for the different stellar masses are given in Table 1. The mass-loss rate as a function of X-ray luminosity and stellar mass is given by (Ercolano et al. 2021; Picogna et al. 2021)

$$\dot{M}_{\mathrm{XEUV}}(M_\star, L_{X,\mathrm{soft}}) = \dot{M}_{\mathrm{XEUV}}(M_\star)\frac{\dot{M}_{\mathrm{XEUV}}(L_{X,\mathrm{soft}})}{\dot{M}_{\mathrm{XEUV}}(L_{X,\mathrm{soft,mean}})}\,, \qquad (4)$$

* E-mail: ercolano@usm.lmu.de

where the mass-loss rate as a function of stellar mass is

$$\dot{M}_{\text{XEUV}}(M_\star) = 3.93 \times 10^{-8} \left(\frac{M_\star}{M_\odot} \right) \qquad (5)$$

and the dependance on the soft component of the X-ray luminosity is given by

$$\dot{M}_{\text{XEUV}}(L_{X,\text{soft}}) = 10^{a_L \exp\left(\frac{(\ln(\log(L_{X,\text{soft}})-b_L)^2}{c_L}\right)+d_L}, \qquad (6)$$

where $a_L = -1.947 \cdot 10^{17}$, $b_L = -1.572 \cdot 10^{-4}$, $c_L = -0.2866$, $d_L = -6.694$, the soft component of the X-ray luminosity is given by

$$L_{X,\text{soft}} = 10^{0.95 \log(L_X)+1.19}, \qquad (7)$$

and the mean component of the X-ray luminosity $L_{X,\text{soft,mean}}$ is the soft X-ray luminosity of a star with a total X-ray luminosity given by the observational relation between stellar mass and X-ray luminosity (see eq. 17, Güdel et al. 2007).

2.2 EUV photoevaporation

We divided the EUV surface mass-loss rate in its diffuse and direct components following Alexander & Armitage (2007)

$$\dot{\Sigma}_{\text{EUV}}(R) = \dot{\Sigma}_{\text{diffuse}}(R) + \dot{\Sigma}_{\text{direct}}(R,t) \cdot f(R), \qquad (8)$$

where $f(R) = 1 + \exp\left(-\frac{R-R_{\text{in}}}{H_{\text{in}}}\right)$ is a smoothing function to avoid numerical problems close to the disc inner edge, $R_{\text{in}}(t)$ is the radius of the inner disc edge, $H_{\text{in}}(t)$ is the disc scale height at the inner edge.

The diffuse component of the EUV surface mass-loss rate is then given by

$$\dot{\Sigma}_{\text{diffuse}}(R) = 2n_0(R)u_l(R)\mu m_H \qquad \text{for } R \geq 0.1R_g, \qquad (9)$$

where the density at the base of the flow is

$$n_0(R) = C_1 \left(\frac{3\Phi_{\text{diff}}}{4\pi\alpha_B R_g^3} \right)^{1/2} \left(\frac{2}{(R/R_g)^{15/2} + (R/R_g)^{25/2}} \right)^{1/5}, \quad (10)$$

the wind launch velocity

$$u_l(R) = c_S A \exp\left[B\left(\frac{R}{R_g} - 0.1 \right) \right] \left(\frac{R}{R_g} - 0.1 \right)^D, \qquad (11)$$

$\mu = 1.35$ the mean molecular weight of the ionized gas, m_H the mass of a hydrogen atom, $C_1 \simeq 0.14$, R_g the gravitational radius, $\alpha_B = 2.6 \cdot 10^{-13}$ is the Case B recombination coefficient for atomic hydrogen at 10^4 K, $c_s = 10$ km s^{-1} the sound speed of the ionized gas, $A = 0.3423$, $B = 0.3612$, $D = 0.2457$, and the stellar diffuse ionizing EUV flux

$$\Phi_{\text{diff}} = \begin{cases} \Phi_{\text{EUV}}\left(\frac{R_{\text{thin}}}{R_{\text{in}}} \right) & \text{if } R_{\text{thin}} < R_{\text{crit}}, \\ \Phi_{\text{EUV}} & \text{otherwise}, \end{cases} \qquad (12)$$

where Φ_{EUV} is the unattenuated stellar ionizing EUV flux (in photons s^{-1}), R_{thin} is the radius at which the disc becomes optically thin in the vertical direction

$$\Sigma_g(R_{\text{thin}}) = m_H \sigma_{13.6\,\text{eV}}^{-1}, \qquad (13)$$

$\sigma_{13.6\,\text{eV}} = 6.3 \cdot 10^{-18}$ cm^2 is the absorption cross-section for ionizing photons, R_{crit} is the critical radius at which the gap opens

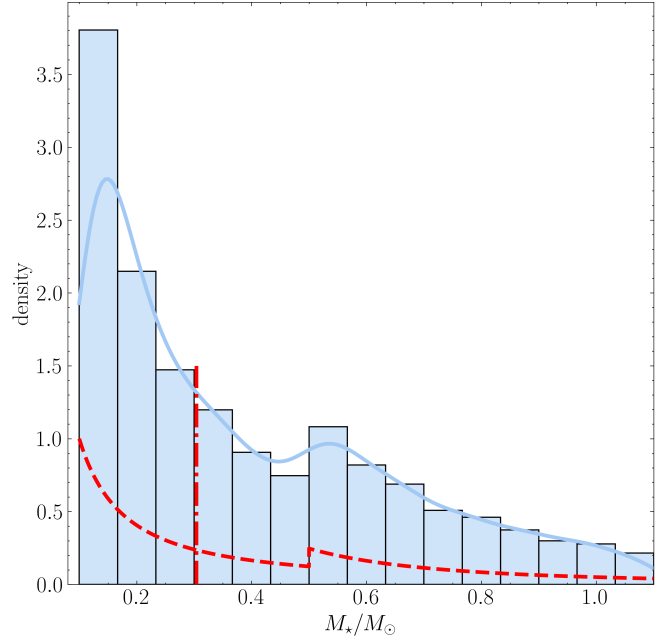$$R_{\text{crit}} = 1.4 \left(\frac{M_\star}{M_\odot} \right) \text{ au}. \qquad (14)$$

Figure 1. Histogram of the stellar mass distribution in our population synthesis, where the KDE is overplotted with a dark blue solid line, the median value of 0.3 M$_\odot$ is marked with a dotted-dashed red line, and the adopted weigthing based on the Kroupa IMF is plotted with a dashed red line.

The direct component of the EUV surface mass-loss rate (defined only for $R > R_{\text{in}}$) is given by

$$\dot{\Sigma}_{\text{direct}}(R,t) = 2C_2\mu m_H c_s \left[\frac{\Phi_{\text{EUV}}}{4\pi\alpha_B (H/R)R_{\text{in}}^3(t)} \right]^{1/2} \left[\frac{R}{R_{\text{in}}(t)} \right]^{-a}, \qquad (15)$$

where $C_2 = 0.235$, $a = 2.42$, H/R is the disc aspect ratio.

2.3 Population synthesis

We assume a initial stellar mass function following Kroupa (2001)

$$\xi(m) \propto m^{-\alpha}, \qquad (16)$$

where $\alpha = 1.3 \pm 0.5$ for $0.08 \leq m/M_\odot < 0.5$ and $\alpha = 2.3 \pm 0.3$ for $0.5 \leq m/M_\odot \leq 1$, from which we obtain the distribution shown in Figure 1 for a sample of 10,000 stars. The adopted weighting of the distribution based on eq. 16 is marked with a dashed red line, and the median stellar mass value given by the dotted dashed red line is ~ 0.3 M$_\odot$.

Güdel et al. (2007) derived an observational relation between the median X-ray luminosities and stellar masses

$$\log_{10}(L_X) = (1.54 \pm 0.12) \log_{10}(M_\star) + (30.31 \mp 0.06), \qquad (17)$$

though a large spread is observed around the mean values, which becomes larger for small mass stars (e.g. Getman et al. 2022). Kuhn & Hillenbrand (2019) took a subsample of the Chandra Orion Ultra-deep Project (COUP, Feigelson et al. (2005); Getman et al. (2005)) and stratified it in 3 stellar mass bins using the Baraffe et al. (1998) evolutionary models. From this sample one can derive a X-ray luminosity function (XLF) as a function of stellar mass, as shown in Figure 2, from which one can see the increase in the median X-ray

Table 1. Parameters for the Surface density profiles in equations 2,3

$M_\star$ [$M_\odot$]	a	b	c	d	e	f	g	$\dot{M}_w$
1.0	−0.6344	6.3587	−26.1445	56.4477	−67.7403	43.9212	−13.2316	3.86446
0.5	−1.2320	10.8505	−38.6939	71.2489	−71.4279	37.8707	−9.3508	1.9046
0.3	−1.3206	13.0475	−53.6990	117.6027	−144.3769	94.7854	−26.7363	1.17156
0.1	−3.8337	22.9100	−55.1282	67.8919	−45.0138	16.2977	−3.5426	0.37588
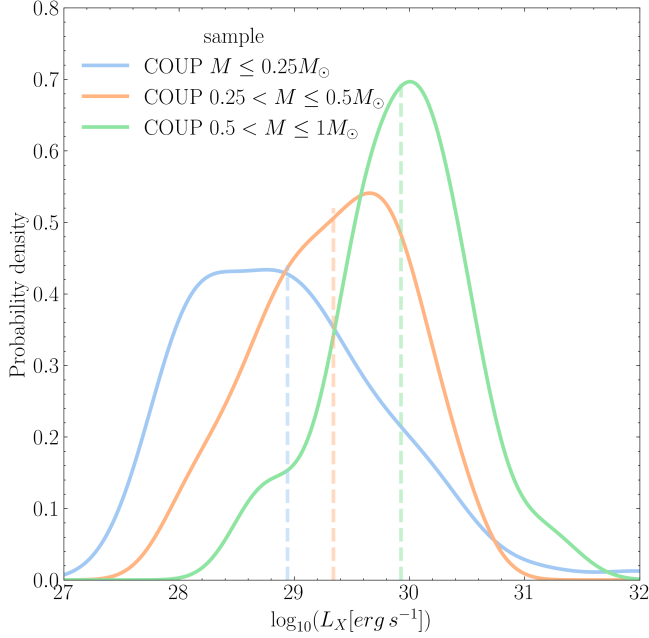
Figure 2. X-ray luminosity function for a representative sample of generic young stellar objects sample of pre-main-sequence stars detected in the Chandra Orion Ultradeep Project (COUP; Feigelson et al. (2005); Getman et al. (2005)), stratified in 3 stellar mass bins as in Kuhn & Hillenbrand (2019).

Figure 3. Histogram of the X-ray luminosity density distribution in the XEUV population synthesis, where the KDE is overplotted with a dark blue solid line and the median value of 29.4 is marked with a dotted dashed black line.
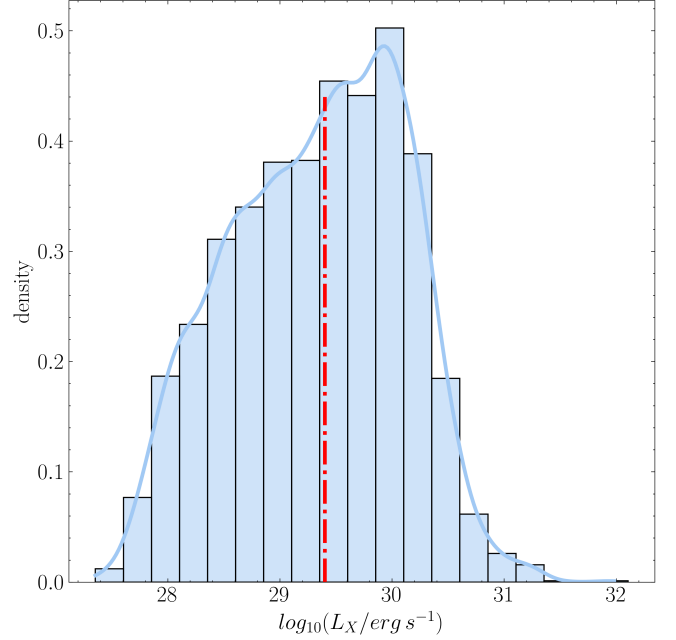
luminosity as a function of stellar mass as well as the increase spreading for lower stellar masses. We then calculated the median stellar mass for the three stellar mass bins in Figure 2 given the adopted IMF, and shifted the XLF distribution to match the given value of the stellar mass. We sampled then the X-ray luminosity given the probability density corrected for the stellar mass and obtained the X-ray luminosity distribution shown in Figure 3 from the 10,000 sampled stellar masses, with a median value of $10^{29.4}$ erg s^{-1} and a spread over 4 orders of magnitude.

The EUV rates are shown to scale with the ratio of incoming ionising flux. However, there is no clear evidence on the origin of the EUV flux. Assuming that the EUV flux has the same origin as the X-ray flux we can then adopt the same scaling relation as eq. 17

$$\log_{10}(\Phi_{EUV}) = 1.54 \log_{10}(M_\star) + 42 \qquad (18)$$

and adopt a small dispersion around the mean value for each stellar mass of 0.25 dex, as shown in Figure 4, which gives a range of ionizing flux from $10^{40} s^{-1}$ to $10^{42.5} s^{-1}$ and a median value of $10^{41.2} s^{-1}$.

We constrained the disc properties in order to match the observed mean disc lifetime of 2-3 Myr (see e.g. Ribas et al. 2014). For the EUV profile we sampled the viscous α and scaling radius R_1 for disc masses ranging from 0.1 to 0.01$M_\star$ for a typical star with median values from our distribution ($M_\star = 0.3 M_\odot$, $\Phi_{EUV} = 10^{41.2}$ s^{-1})

and then we selected only the ones that were giving a correct disc life-time and obtained a best linear fit given by:

$$R_1 = 60.4\alpha + 3009.7 M_d [M_\star] + 226.6 \qquad [\text{au}]. \qquad (19)$$

We then sampled the whole stellar mass range and obtained the full sampling of the parameter space shown in Figure 5. For the XEUV profile we realized that the disc evolution was primarily driven by the internal photoevaporation rather than the disc properties, thus we chose to sample uniformly the parameter space for the disc properties and fix only the disc mass to 0.1$M_\star$ as this is a reasonable value of the initial disc mass when the disc self-gravity stops being the driver of disc evolution and the approximation of a viscously evolving disc is reasonable. We summarize the parameter space probed in Table 2.

3 RESULTS

Figure 6 shows the accretion rates as a function of time for a population synthesis of 10,000 discs sampled as described in the previous section. Overplotted with blue dots of variable size (based on their stellar mass) is the population of low accretors from Thanathibodee et al. (2023), and the observational limit of the He I λ10830 marked with a black dashed line at 10^{-11} M$_\odot$ yr^{-1}. One can immediately see that while the XEUV profile catches all the observed data points

Table 2. Parameters for the population synthesis calculations.

name	viscosity $\log_{10}(\alpha)$	r1 au	disc mass $M_\star$	stellar mass $M_\odot$	stellar flux (Φ_{EUV}, L_X)
EUV	Fig. 5	Fig. 5	Fig. 5	Fig. 1	Fig. 4
XEUV	[-4, -2]	[10, 100]	0.1	Fig. 1	Fig. 3
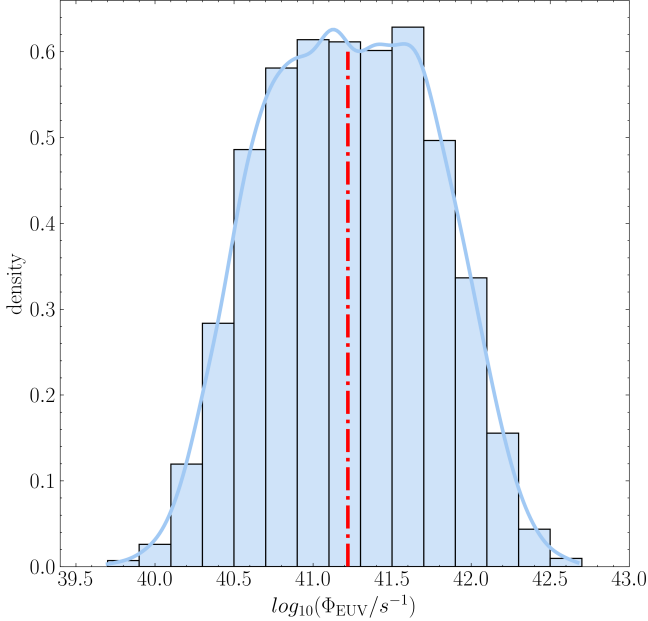
Figure 4. Histogram of the ionizing flux density distribution in the EUV population synthesis, where the KDE is overplotted with a dark blue solid line and the median value of 41.2 is marked with a dotted dashed black line.

in the region with high density ($> 10^{-2}$), while the EUV cannot explain the data for the older star-forming regions (Orion OB1a and Upper Sco). Furthermore the observational data points lie in the upper region of the distribution, even though they are a sample of the low-accretors population. This means that the bulk of the discs in the studied star forming regions covers a region not explained by the EUV photoevaporation profiles.

Another way to show the results, and avoid the errors related to the age determination of star forming regions is to plot the accretion rates as a function of the star forming region disc fractions (see Figure 7). In a similar way here the data points for the low-accretors lie all in the region with low probability density or not explained by the current EUV models (left panel). The situation is significantly different looking at the XEUV population (right panel) where the data points sit in the bulk of the distribution, with small mass stars (small dots) covering the lower part of the high density distribution and the bigger stars the top part. This is expected from the observationally derived relation between accretion rate and stellar masses, that shows a sharp increase of the accretion rate as a function of stellar mass with a broken power law (Alcalá et al. 2017).

We plotted in Figure 8 the histogram of the accretion rate distribution for the EUV (in blue) and XEUV (in green) populations. We overplotted as well the median accretion rates in dotted-dashed blue and green line respectively, and the median accretion rate for the observed population of low-accretors with a dotted-dashed black line. From this one can directly visualize how the median of the XEUV

population and the observed low-accretors is very similar, while it is close to the high-accretor wing of the EUV distribution.

We compared finally the distribution of disc fractions as a function of age, calculated as the time at which the accretion rate drops below 10^{-11} $M_\odot$ yr^{-1} in our population synthesis with the observed distribution of disc fraction. As expected the EUV distribution fits perfectly, as we choose the parameter space in order to fit it for the median stellar mass and EUV ionizing field. The XEUV distribution is also very accurate in describing the observed star forming region population with the only constraint of an initial disc mass of 0.1 $M_\star$.

3.1 Mass dependent results

The results shown in the previous section assume a well-sampled IMF, which implies that objects at the lower end of the mass range are the most abundant. However the sample of low accretors of Thanathibodee et al. (2023) includes only 24 objects with masses ranging between 0.1 and 1.39 $M_\odot$. The majority of objects have masses between 0.5 and 0.6 $M_\odot$, resulting in a significant different stellar mass function with respect to the adopted IMF, as shown in Figure 10.

The accretion rate values reported by T22 do not show any obvious correlation with the object mass. In Figures?? to??? we show the accretion rate probabilities for our populations when we restrict the mass ranges to low (0.1-0.3), intermediate (0.3-0.6), high (0.7-0.9). how does the picture change for the individual masses ranges?.

We find....

3.2 Low-accretors variability

Fang et al. (2023) obtained the accretion rate of a large sample in Upper Sco adopting high-resolution optical spectra from Hα line profiles. Comparing their results with the ones measured for the same star forming region by Manara et al. (2020), fitting simultaneously the stellar photosphere and Balmer continuous emission, they find a large spread (see their Figure 29) going to more than one order of magnitude, especially for the population of low-accretors. Comparing the low accretors with the ones derived fitting the He I λ10830 line profiles in Thanathibodee et al. (2023) they found further differences in disc classification and accretion rates. This points towards a general difficulty in classifying low accretors based on line profiles, and their intrinsic variability that should be studied further.

4 CONCLUSIONS

ACKNOWLEDGEMENTS

DATA AVAILABILITY

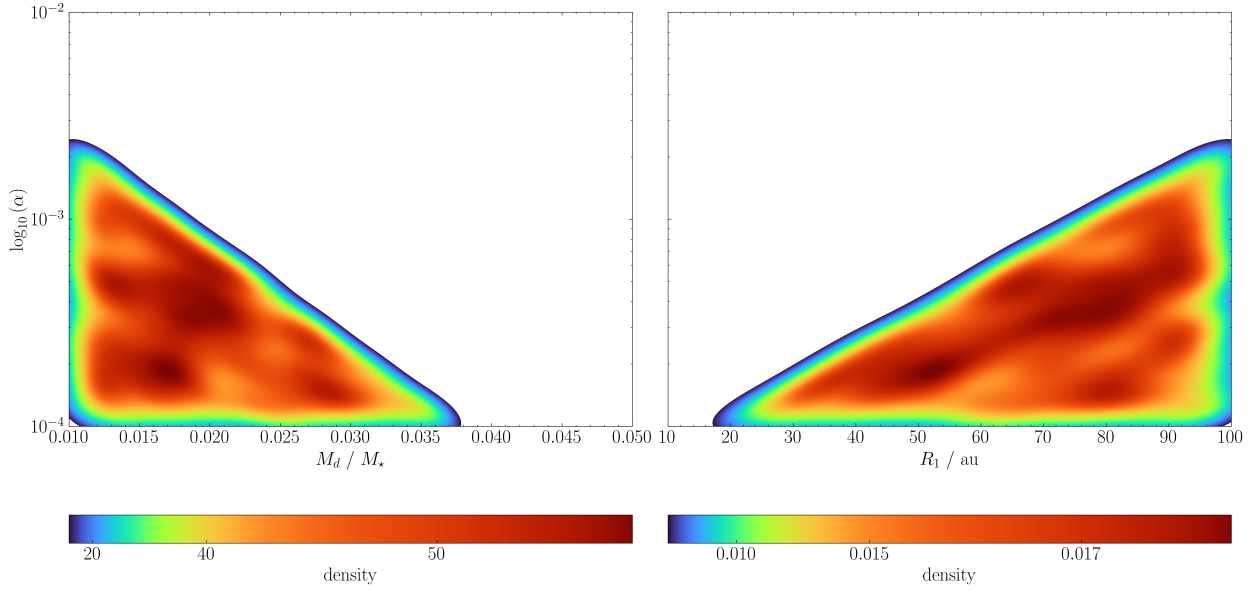The data for the population synthesis calculations is available at .....

Figure 5. KDE plot of the alpha - disc mass (left) and alpha-r1 (right) parameters that were adopted in the EUV population synthesis in order to have a disc life-time compatible with the observationally derived one.
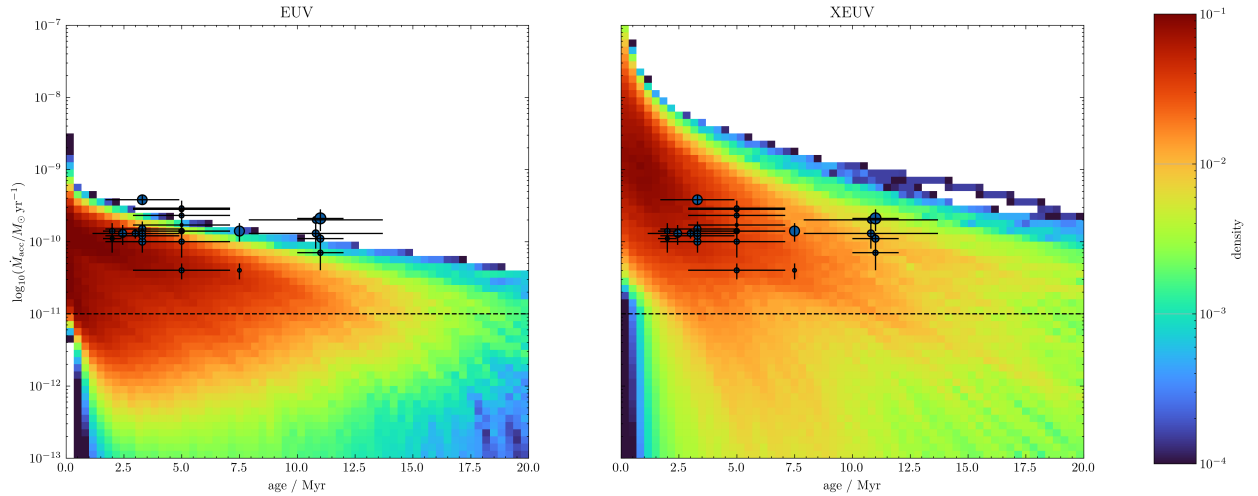

Figure 6. Synthetic populations showing the accretion rates as a function of age. The colors show the probability of finding an object of a given age accreting at a given rate (see text for details). Left panel: Discs are dispersed by EUV photoevaporation; right panel: discs are dispersed by X-ray photoevaporation. The low-accretors population is overplotted with blue dots with variable size increasing by the stellar mass.

REFERENCES

Alcalá J. M., et al., 2017, A&A, 600, A20

Alexander R. D., Armitage P. J., 2007, MNRAS, 375, 500

Baraffe I., Chabrier G., Allard F., Hauschildt P. H., 1998, A&A, 337, 403

Ercolano B., Rosotti G., 2015, MNRAS, 450, 3008

Ercolano B., Picogna G., Monsch K., Drake J. J., Preibisch T., 2021, MNRAS, 508, 1675

Fang M., Pascucci I., Edwards S., Gorti U., Hillenbrand L. A., Carpenter J. M., 2023, ApJ, 945, 112

Feigelson E. D., et al., 2005, ApJS, 160, 379

Getman K. V., et al., 2005, ApJS, 160, 319

Getman K. V., Feigelson E. D., Garmire G. P., Broos P. S., Kuhn M. A., Preibisch T., Airapetian V. S., 2022, ApJ, 935, 43

Güdel M., et al., 2007, A&A, 468, 353

Kroupa P., 2001, MNRAS, 322, 231

Kuhn M. A., Hillenbrand L. A., 2019, ApJ, 883, 117

Lesur G., et al., 2022, arXiv e-prints, p. arXiv:2203.09821

Lynden-Bell D., Pringle J. E., 1974, MNRAS, 168, 603

Mamajek E. E., 2009, in Usuda T., Tamura M., Ishii M., eds, American Institute of Physics Conference Series Vol. 1158, Exoplanets and Disks: Their Formation and Diversity. pp 3–10 (arXiv:0906.5011), doi:10.1063/1.3215910

Manara C. F., et al., 2020, A&A, 639, A58

Monsch K., Ercolano B., Picogna G., Preibisch T., Rau M. M., 2019, MNRAS, 483, 3448

Pascucci I., Cabrit S., Edwards S., Gorti U., Gressel O., Suzuki T., 2022, arXiv e-prints, p. arXiv:2203.10068

Picogna G., Ercolano B., Owen J. E., Weber M. L., 2019, MNRAS, 487, 691

Picogna G., Ercolano B., Espaillat C. C., 2021, MNRAS, 508, 3611

Ribas Á., Merín B., Bouy H., Maud L. T., 2014, A&A, 561, A54

Skrutskie M. F., Dutkevitch D., Strom S. E., Edwards S., Strom K. M., Shure M. A., 1990, AJ, 99, 1187

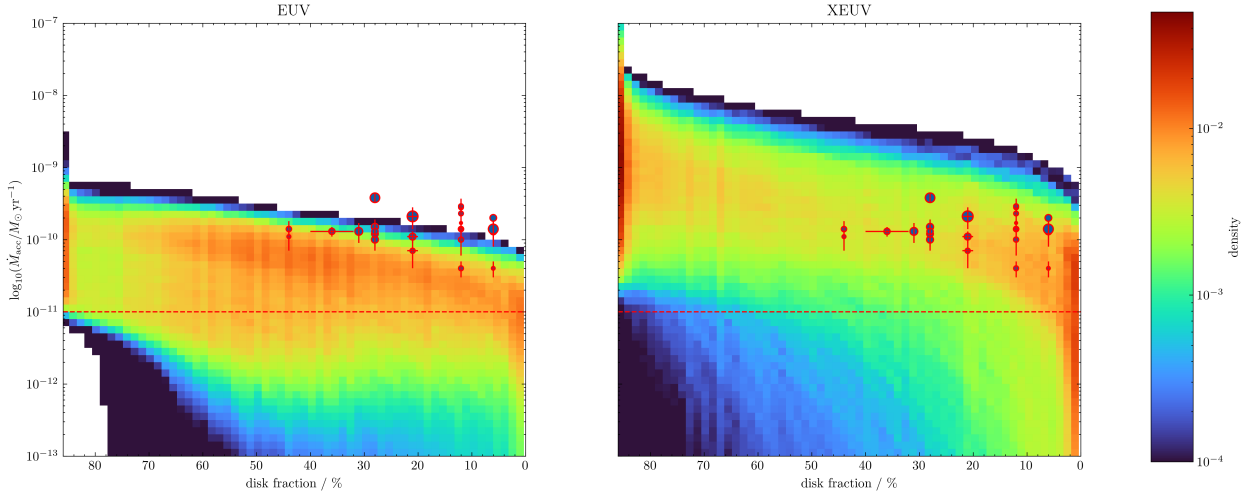Thanathibodee T., Calvet N., Hernández J., Maucó K., Briceño C., 2022, AJ,

Figure 7. Synthetic populations showing the accretion rates as a function of disc fraction. The colors show the probability of finding a disc of a given accretion rate in a star forming region with a given disc fraction (see text for details). Left panel: Discs are dispersed by EUV photoevaporation; right panel: discs are dispersed by X-ray photoevaporation. The low-accretors population is overplotted with blue dots with variable size increasing by the stellar mass.
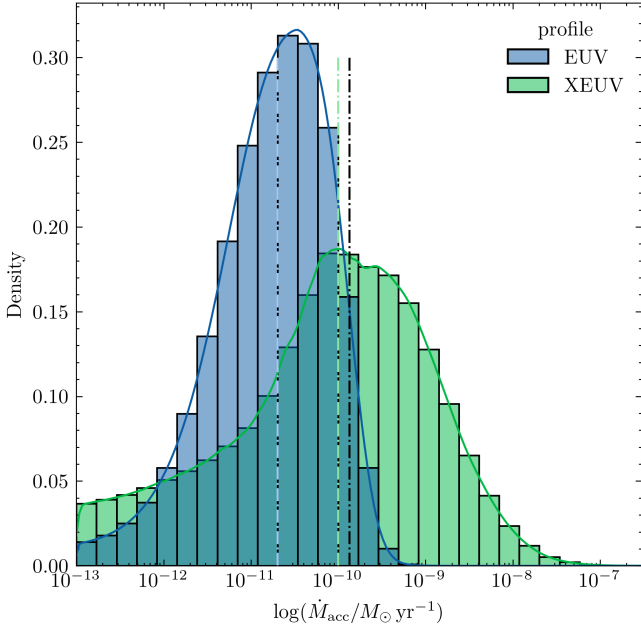

Figure 8. Histogram of the accretion rate density distribution in the EUV (blue) and XEUV (green) population synthesis. The KDE is overplotted with a blue and green solid line for the EUV and XEUV distributions respectively, and the median values are plotted with dotted-dashed lines. For direct comparison the median accretion rate of the low-accretors population is plotted with a black dotted-dashed line.

163, 74

Thanathibodee T., Molina B., Serna J., Calvet N., Hernández J., Muzerolle J., Franco-Hernández R., 2023, ApJ, 944, 90

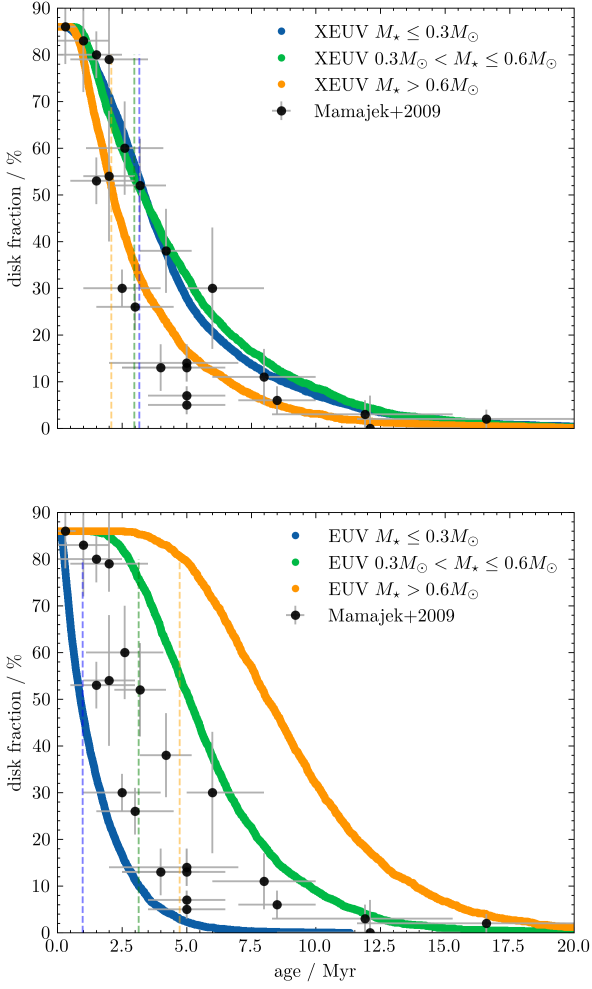This paper has been typeset from a TEX/LATEX file prepared by the author.

Figure 9. Disc fraction as a function of disc lifetime for the XEUV (top panel) and EUV (bottom panel) synthetic populations compared with the observational data from Mamajek (2009), divided in 3 stellar mass bins. The median disc lifetime are plotted with dashed vertical lines. The median disc life-time increases with stellar mass for the EUV models, while it decreases for the XEUV models.
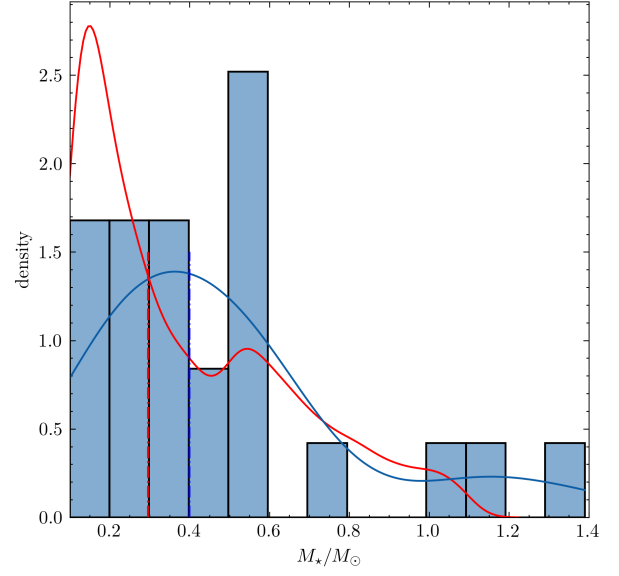

Figure 10. Stellar mass distribution of the low-accretor population in Thanathibodee et al. (2023) with overplotted KDE in a solid blue line, compared with the IMF adopted in this work shown with a red solid line. The median values of the two distributions are shown with blue and red dotted-dashed line, respectively.